Q. J. R. Meteorol. Soc. (1999), **125**, pp. 1039–1058

Electrodynamic trapping and manipulation of ice crystals

By BRIAN D. SWANSON*, NEIL J. BACON, E. JAMES DAVIS and MARCIA B. BAKER
University of Washington, Seattle, USA

(Received 22 September 1997; revised 16 June 1998)

SUMMARY

We have developed a double-ring double-disk electrodynamic balance with humidity control provided by an internal thermal diffusion chamber to study several atmospherically important processes involving 10–200 μm ice particles. The balance constants needed to quantify the particle size and mass were determined by a three-dimensional relaxation-method calculation of the non-axisymmetric electric fields, and by experimental measurement of the onset of particle stability using polystyrene latex microspheres of known size and mass. We have levitated frost particles of various shapes and sizes under a range of atmospherically relevant temperature and humidity conditions. The measured mass changes during growth and sublimation are consistent with predictions based on vapour and thermal diffusion to equivalent spheres. The electrodynamic balance is shown to be a useful tool for exploring single particle growth and sublimation rates, and for measuring their light-scattering characteristics.

KEYWORDS: Electrodynamic balance Frost-particle growth and sublimation Ice-crystal levitation

1. INTRODUCTION

Laboratory observations of the properties and evolution of ice particles under atmospheric temperature and humidity conditions can provide useful information for climate studies (Baker 1997). However, most laboratory experiments studying ice crystals have involved substrates (Lamb and Hobbs 1971; Lamb and Scott 1972; Beckmann 1982; Beckmann and Lacmann 1982; Sei and Gonda 1982), where heat and vapour flows are quite unlike those in the atmosphere, or have focused on clouds of particles in wind tunnels at water saturation (Ryan *et al.* 1976; Takahashi *et al.* 1991), so that individual particles could not be followed. Moreover, there have been few sublimation-rate measurements (Takahashi *et al.* 1991).

In this paper we report the construction and use of a specially designed electrodynamic balance (EDB) to measure atmospherically relevant properties of single levitated ice particles. An electrodynamic balance levitates and traps a charged particle by the simultaneous application of direct-current (dc) and alternating-current (ac) potentials. The dc field counteracts the force due to gravity and any other vertical forces on the particle, and the ac potential dynamically stabilizes the particle at the balance centre, or null point, by exerting a restoring force proportional to the distance from the null point. Paul and Steinwedel (1953) introduced the electric mass filter, or quadrupole trap, and since then electrodynamic balances with a variety of electrode configurations have been used to study atomic ions, microparticles, aerosol chemistry, and heat and mass transfer to aerosols and liquid drops. The classical bihyperboloidal electrode configuration of Wuerker *et al.* (1959) has been widely used for such studies (see reviews by Davis (1992) and (1997)). Since, in the EDB environment, ventilation effects are minimal we limit our focus to relatively small particles and to processes in which ventilation effects are not important.

The EDB constructed for this study has a double-ring double-disk electrode configuration and incorporates an internal thermal diffusion chamber, an angular light-scattering detector, and observation ports for imaging the levitated particle. It is demonstrated here that the EDB is useful for maintaining ice crystals under both supersaturated and subsaturated conditions, and that growth, sublimation and morphological changes of single ice particles can be measured using four techniques—optical microscopy, particle stability characteristics, angular light-scattering and balance voltage measurements. Since the

* Corresponding author: Geophysics Program, University of Washington, Box 351650, Seattle, WA 98195-1650, USA. e-mail: brian@geophys.washington.edu

particles in the balance are charged and are situated in electric fields it is, therefore, necessary to examine the possibility that the electric fields in our balance may be affecting the processes we are studying.

Both crystal habit and crystal size can be affected by growth in an ambient electric field of strength 10^3 V cm^{-1} (Bartlett *et al.* 1963; Crowther and Saunders 1973; Evans 1973). However, the ambient dc fields at the particle location in our balance are about 100 V cm^{-1} or lower—at least an order of magnitude lower than those found to modify the growth and sublimation (g/s) rates. (The maximum ac field 0.1 cm from the particle location is also about 100 V cm^{-1}.) For this ambient field, the maximum field at the tips of an ellipsoid of length 100 μm and aspect ratio 10:1 is $E_{max} \approx 240$ V cm^{-1}, causing an induced charge density near the tips of $\approx 2 \times 10^{-11}$ C cm^{-2}, or total charge on half the particle of about 3×10^{-15} C. This is small compared with the charges required to trap the particles ($\approx 10^{-13}$ C) and with the charges acquired by small ice particles in thunderstorms and in laboratory studies of electrification (Jayaratne *et al.* 1983; Baker *et al.* 1987). No effects on growth rate of the surface charge density associated with the net or induced charge have been previously reported, and we observed no such effect here.

In addition to the initial charge on the levitated particles, it has been established that ice particles and drops acquire a small amount of charge during g/s (Dong and Hallett 1992; Cross and Speare 1969). Measured charging rates are on the order of 10^{-16} A cm^{-2}, positive charging accompanying growth and negative charging occurring during evaporation/sublimation. A spherical 20 μm ice particle charging at this rate would acquire about $\approx 3 \times 10^{-21}$ C s^{-1}, so for trapping times of less than one day the net charge acquired due to phase change is small compared with the trapping and the induced charge. We conclude from these considerations that the artifacts introduced into our measurements by electrical effects are minimal and do not modify the results reported here in measurable ways.

In the next section we describe our apparatus and in section 3 we explain our estimates of the electrostatic-potential, temperature, and humidity distributions in the chamber. In section 4 we describe our experimental procedure, the particle mass determinations and the calibrations of the relevant parameters. We describe our results in section 5, and summarize our plans for future application of the EDB technique in the last section.

2. EDB AND THERMAL DIFFUSION CHAMBER

Our balance, illustrated in Fig. 1, consists of a cylindrical diffusion chamber with polyvinyl chloride (PVC) side walls (Swanson and Baker 1995). Single, electrically charged ice particles were levitated and stabilized at the centre of the chamber by a superposition of dc and ac electric fields. The dc potential (ranging from 10–700 V) was applied to the two copper endcap electrodes while the ac potential (from 500–2300 V peak at 15–300 Hz) was applied to the stainless steel ring electrodes. The ac electrodes were coated with a surfactant to inhibit ice nucleation.

Optical windows mounted on the sides, top and bottom of the chamber allowed for illumination, optical and video telemicroscopy, angular scattering measurements and ice-particle insertion. The particle was illuminated either by a broad-spectrum source or a 10 mW polarized He–Ne laser. The optical particle size and shape determinations were made with bright-field incandescent illumination using two telemicroscopic video cameras mounted at the top and side of the chamber. The zoom telemicroscopic lenses attached to the cameras provided a magnification from 200× to 1400× for both transverse and longitudinal views of the particle. The transverse and longitudinal images of the particle were electronically combined so that both views were recorded side-by-side on video tape and digitally with a frame-grabber. Optical resolution was about 1 μm per pixel. A 2.54 cm

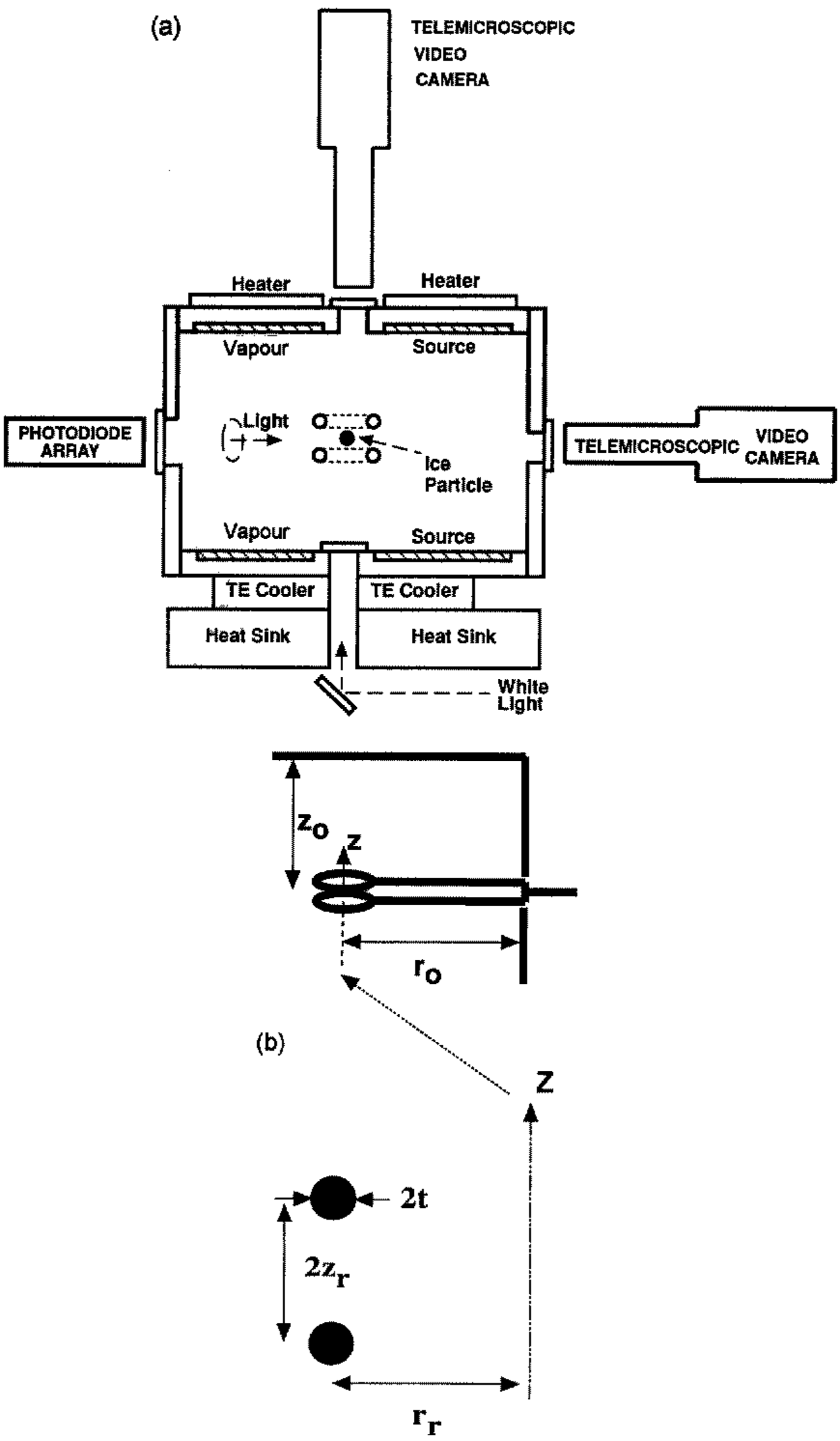

Figure 1. (a) Schematic diagram of double-ring double-disk electrodynamic balance built for these experiments, (b) the ac electrode configuration (see text for explanation of symbols).

long 1024-element linear photodiode array was mounted on the side wall of the chamber as indicated in Fig. 1(a). This array, interfaced to a computer, measured the light-scattering intensity over the scattering angle range 15° to 85° every 0.3 s. Measurements of the light-scattering phase function from non-spherical ice particles will be discussed in a future paper.

The balance was situated in a cold room that controlled the ambient temperature down to −30°C. Supersaturated conditions near the centre of the chamber were maintained by a vertical-gradient thermal diffusion chamber consisting of vapour sources mounted on the inside surfaces of the top and bottom end-cap electrodes. In a thermal diffusion chamber (first described by Langsdorf (1936) and (1939)) operating at $T < 0$°C, water vapour diffuses between the upper warmer vapour source and the lower colder ice surface. In our chamber, the top and bottom humidity sources consisted of filter paper soaked in DI water ($T > 0$°C) or frozen filtered de-ionized (DI) water ($T < 0$°C), maintained at temperatures T_{top} and T_{bottom} with heaters and/or Peltier devices mounted at each vapour source. Thermistors mounted at the vapour sources and in the chamber walls monitored the temperatures which, along with the voltages and ac frequency, were recorded every second by computer.

3. Electric-potential, temperature and humidity distributions

The static and oscillatory components of the electric potential, and the temperature and humidity distributions in the chamber (in the absence of the light source) are, to a good approximation, determined by solution of Laplace's equation subject to appropriate boundary conditions on the ac and dc electrodes and their support rods, the chamber walls, and the top and bottom humidity sources. Various mathematical methods have been used to find the electric field in axisymmetric electrodynamic-balance geometries. Expansions in terms of harmonic polynomials (Frickel *et al.* 1978; Hartung and Avedisian 1992), ring-charge simulation techniques (Sloane and Elmoursi 1987; Davis *et al.* 1990), and a numerical Green's function method (Loyalka *et al.* 1995) have been developed for different electrode geometries. We have used a three-dimensional relaxation method, on a $\sim 10^6$ point grid throughout the balance chamber, to calculate these fields. This method explicitly includes the ring electrodes with non-axisymmetric support-rod configuration of the balance (Aardahl *et al.* 1997). In the following paragraph we discuss our calculation of the electric potentials in some detail.

(*a*) *The electric fields*

In the double-ring double-disk EDB configuration of Fig. 1, the balance walls enclose a cylindrical cavity with radius r_o and height $2z_o$. The top and bottom end caps of this cavity are disks to which the dc potential $2V_{dc}$ is applied. Near the centre of the cavity a pair of ring electrodes with radius r_r are positioned a distance z_r above and below the mid plane ($z = 0$), and an ac potential $V_{ac}\cos(\omega t)$ with frequency $f = \omega/2\pi$ is applied to both rings. The electric fields throughout the chamber are obtained by solving for the potential $\psi = \psi_{dc} + \psi_{ac}$, with $\mathbf{E} = -\nabla\psi$. For sufficiently slow temporal variations of the applied ac potential, and neglecting the charge of the levitated particle, the potential $\psi(\mathbf{r}_s) = \psi(r, \phi, z)$ at all points $\mathbf{r}_s$ within the chamber satisfies Laplace's equation with the boundary conditions

$$\begin{aligned} V_{top} &= \psi(z = z_o) = V_{dc} \\ V_{bottom} &= \psi(z = -z_o) = -V_{dc} \\ V_{ring} &= V_{ac}\cos(\omega t). \end{aligned} \tag{1}$$

TABLE 1. THE DIMENSIONS OF THE ELECTRODYNAMIC BALANCE CHAMBER AND THE ELECTRODE (mm) FOR THE TWO CONFIGURATIONS $\mathscr{A}$ AND $\mathscr{B}$ (SEE FIG. 1 AND TEXT FOR EXPLANATION OF SYMBOLS)

Configuration	r_o	r_r	t	z_r	z_o
$\mathscr{A}$	22.85	5.95	0.79	2.39	19.60
$\mathscr{B}$	22.85	5.70	0.83	1.38	19.60

We used an analytic Green's function method to ascertain that the electric potentials were close to zero at the inner surfaces of the dielectric side walls. The dielectric boundary at $r = r_o$ was, therefore, approximated as a constant potential surface with $\psi(r = r_o) = 0$. The relaxation procedure was initiated by setting rings, support rods and top and bottom surfaces to the appropriate voltage, and by setting the potential at every other grid point to zero. The potential at each grid point was then adjusted until the solution converged at all points. Since, for our purposes, it is sufficient to know the potentials at small displacements r, z from the null point, or the point where $\psi_{dc}(r, z) = 0$, we fit the solutions to the form

$$\psi_{dc}(r, z, \phi) = V_{dc}\frac{z}{z_o}\left\{C_0 + a_{11}\frac{r\cos\phi}{z_o} + a_{21}\frac{r^2\cos(2\phi)}{{z_o}^2}\right\}, \tag{2}$$

and

$$\psi_{ac}(r, z, \phi, t) = V_{ac}\cos(\omega t)\left\{C_{-1} - \frac{C_1}{z_o^2}\left(z^2 - \frac{r^2}{2}\right) + a'_{11}\frac{r}{z_o}\cos\phi + a'_{21}\frac{r^2}{{z_o}^2}\cos(2\phi)\right\}, \tag{3}$$

where the coefficients C_{-1}, C_0, C_1, a_{11}, a'_{11}, a_{21}, and a'_{21} are constants to be determined. Note that the terms in $\cos\phi$ do not appear in axisymmetric balances, and arise here because of the radial support rods located at $\phi = 0$.

The distortion of the potential by the support rods is evident in Fig. 2 from the ridge that extends radially out from the central depression. Figure 3(a) shows the ac and dc potentials along the axis of the balance, $\hat{z}$. The effect of the ring electrodes located at $\pm z_r$ flattens the dc potential near the centre of the balance. Figure 3(b) shows the ac potential at the balance mid plane ($z = 0$) in the direction parallel to the ac electrode support rods ($\phi = 0$ and 180°), $\hat{y}$, and in the direction perpendicular to the ac electrode support rods ($\phi = 90$ and 270°), $\hat{x}$. While the ac potential along the $\hat{x}$ axis is symmetric about $r = 0$, the asymmetry of the potential caused by the rods is clearly evident here along the $\hat{y}$ axis. The dc and ac potentials were calculated for the two electrode configurations $\mathscr{A}$ and $\mathscr{B}$ shown in Table 1. Fits of these potentials to Eqs. (2) and (3) give the best-fit parameters listed in Table 2.

(*b*) *Temperature and humidity estimation*

We are not able to measure the temperature and humidity directly in the immediate vicinity of the levitated particle while the particle is in place. For the aspect ratio (≈ 1) of our balance, the temperature and humidity profiles at the side walls can significantly influence

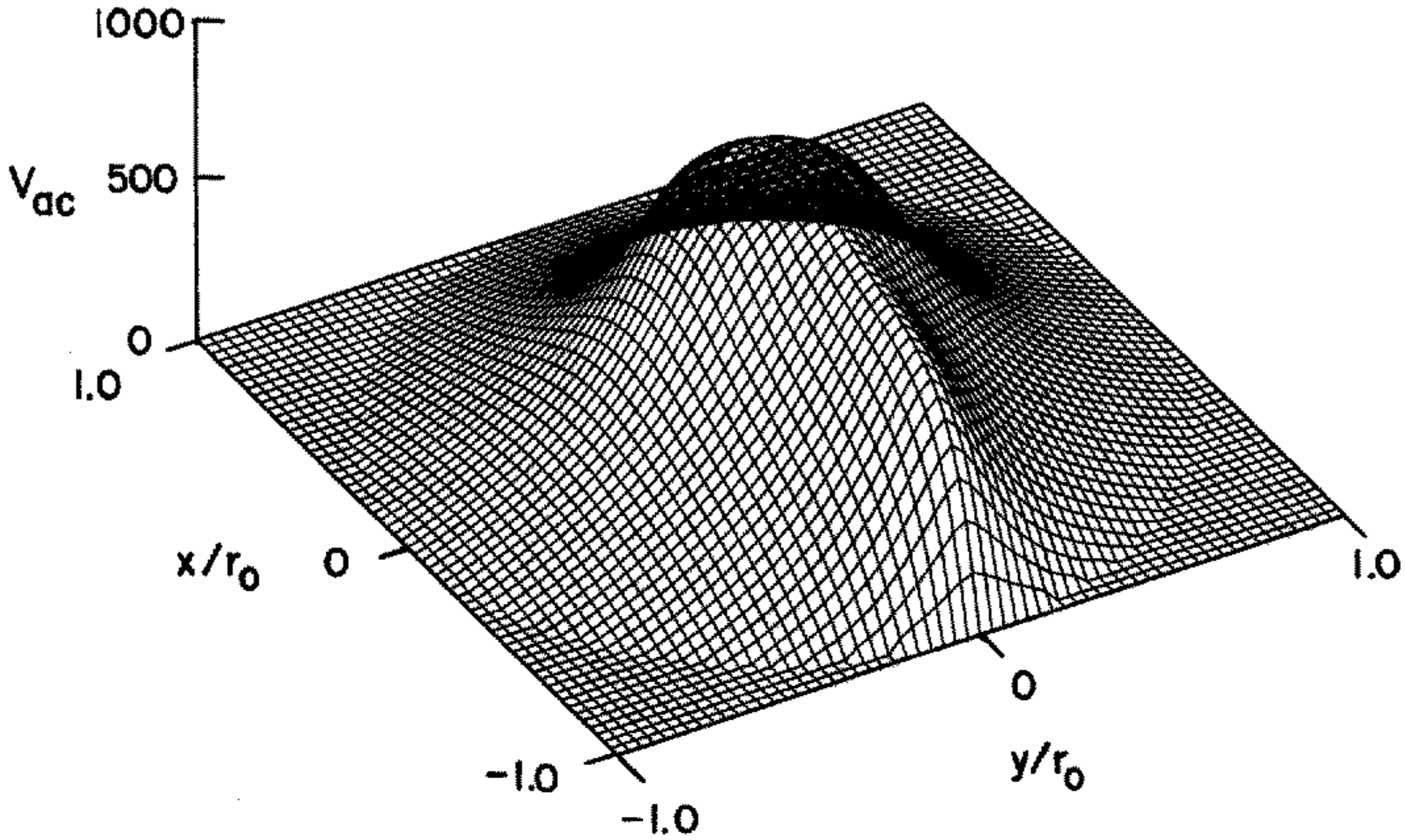

Figure 2. Laplace relaxation-method calculation results for the distribution in the (x, y) plane of the ac electric potential, V_{ac}, in the electrodynamic balance, displayed in three-dimensional form ($V_{top} = -V_{bottom} = 0$, $V_{top-ring} = V_{bottom-ring} = 1000$ V) (see text for explanation of symbols).

TABLE 2. BALANCE COEFFICIENTS FOR THE TWO ELECTRODE CONFIGURATIONS $\mathscr{A}$ AND $\mathscr{B}$ GIVEN IN TABLE 1, DETERMINED FROM BEST-FIT CALCULATIONS AND FROM EXPERIMENTAL RESULTS

Configuration	Calculation results from theory						Experimental results			
	C_{-1}	C_0	C_1	a'_{11}	a'_{21}	C_1/C_0	A_0	A_1	A_2	C_1/C_0
$\mathscr{A}$	0.78	0.63	2.18	−0.081	0.22	3.5	0.45	0.25	0.225	3.6
$\mathscr{B}$	0.77	0.69	4.23	−0.056	0.21	6.1	0.45	0.49	1.25	5.9

The coefficients C_{-1}, C_0, C_1, a'_{11} and a'_{21} are defined in Eqs. (2) and (3), and A_0, A_1 and A_2 are defined in Eq. (8). For both electrode configurations the relaxation calculation gives $a_{11} \sim 0$ and $a_{21} \sim 0$.

the conditions at the centre of the chamber (Elliott 1971; Katz and Mirabel 1975; Tomlinson and Fukuta 1979). In addition, the effects of the ac electrodes near the centre of the chamber must be taken into account. We estimate the temperature and humidity distributions in the absence of the light source ($T_0(r, z)$, $\rho_{v,0}(0, 0)$) by two methods: (i) the relaxation method described above (using the measured temperatures and saturated conditions on all surfaces) and (ii) a simple analytic solution that neglects the effects of the ac ring electrodes and support rods. Comparison of the calculated temperature distributions using these two methods shows the solutions agree to within 0.1°C when the temperature distribution is symmetric about the horizontal ($z = 0$) plane through the balance centre. However, the difference in the calculated temperatures at the particle position is greater when the distribution is asymmetric. The results presented in this paper do not depend on accurate determination of the temperature or the supersaturation at the centre of the chamber; our estimates of these parameters are discussed in section 5.

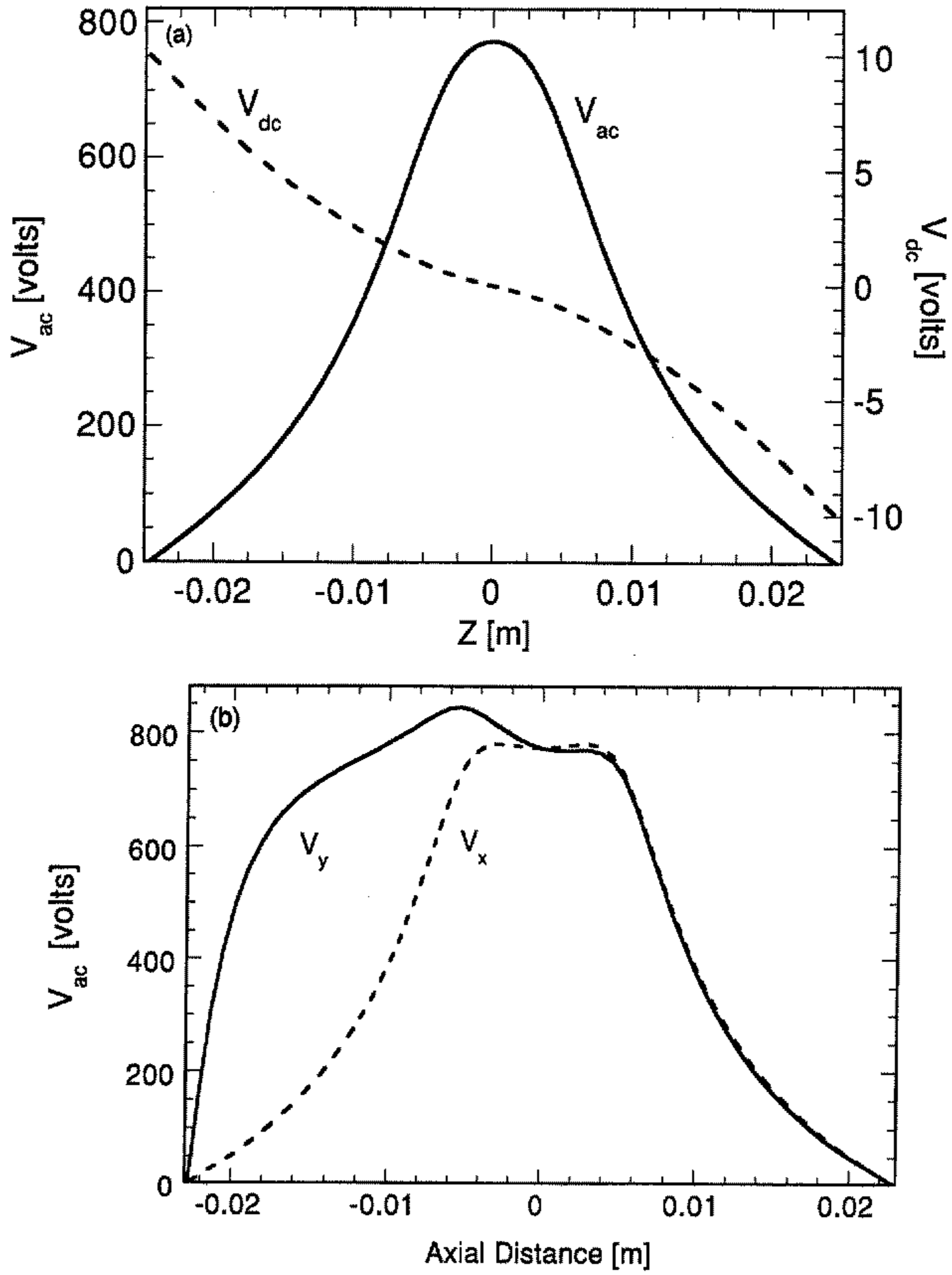

Figure 3. Laplace relaxation-method calculations for the electric potentials, V_{ac} and V_{dc}, along the $\hat{z}$, $\hat{x}$ and $\hat{y}$ directions (see text). (a) V_{ac} (solid line) and V_{dc} (dotted line) along the $\hat{z}$-axis (with $r = 0$) and (b) V_{ac} along the $\hat{x}$ and $\hat{y}$ direction at $z = 0$.

4. Mass and charge determination

The equation of motion of a particle of mass m and charge q levitated at position $\mathbf{r}_s(r, \phi, z)$ from the nullpoint is

$$m\frac{\mathrm{d}^2\mathbf{r}_s}{\mathrm{d}t^2} + K_d\frac{\mathrm{d}\mathbf{r}_s}{\mathrm{d}t} = m\mathbf{g} + q(\mathbf{E}_{dc} + \mathbf{E}_{ac}) + \mathbf{F}_{ext}, \tag{4}$$

where $\mathbf{g}$ is the gravitational acceleration, $\mathbf{E}_{dc}$ and $\mathbf{E}_{ac}$ are the applied dc and ac electric fields, and $\mathbf{F}_{ext}$ is any other external force on the particle. For a small particle of characteristic size a in the Stokes regime (i.e. for Reynold's number $Re \ll 1$, appropriate for the particles discussed here) the drag coefficient $K_d = 6\pi a\xi\mu$, where μ is the viscosity of the surrounding air, and ξ is a shape factor (for non-spherical particles) that depends on the particle orientation with respect to the direction of travel ($\xi = 1$ for Stokesian motion of spherical particles).

To extract the mass m and charge q of the particle from balance voltage and ac frequency measurements, we separate the oscillatory and non-oscillatory parts of Eq. (4). We assume $\mathbf{F}_{ext} = 0$ throughout and derive the fields from the potentials given in Eqs. (2) and (3). The balance of the axisymmetric time-independent forces of Eq. (4) gives

$$\frac{m}{q} = \frac{E_{dc,z}}{g} = -\frac{V_{dc}C_0}{gz_o}, \tag{5}$$

where C_0 is defined in Eq. (2).

The time-varying vertical and radial components in Eq. (4) can be written in a non-dimensional form known as Mathieu's equation (Abramowitz and Stegun 1972; Frickel *et al.* 1978),

$$\frac{\mathrm{d}^2X_i}{\mathrm{d}\tau^2} - \{\alpha^2 + 2Q_i\cos(2\tau)\}X_i = 0, \qquad i = 1, 2 \tag{6}$$

where $X_1 = r$, $X_2 = z$, $Q_2/2 = \beta = -Q_1$, $\tau \equiv (\omega t)/2$, and

$$\alpha \equiv \frac{6\pi a\xi\mu}{m\omega} \qquad \beta \equiv -\frac{2gV_{ac}C_1}{z_o\omega^2V_{dc}C_0}. \tag{7}$$

Mathieu's equation has been studied extensively (Frickel *et al.* 1978; Hartung and Avedisian 1992). The regions of stable and unstable orbits can be mapped as regions in the α, β plane. The boundary between these regions is called the instability envelope, and has been calculated for spherical particles. Particles originally executing stable orbits begin to oscillate violently as the instability envelope is crossed, usually induced by varying V_{ac} and/or ω. In practice, it is the vertical (z) instability that first appears (Hartung and Avedisian 1992) and which we utilize for size determination; our neglect of the radial (r) and azimuthal ($\cos\phi$) terms is thus justified. Spherical particles of known mass can be used to determine the instability envelope for each electrode configuration. Comparison with the theoretical values then provides a check on the calculated value of the parameter C_1/C_0, the only unknown in Eq. (7). This ratio can then be used to determine the (unknown) mass and the charge of any other particle levitated in the same balance from measurements of V_{dc}, V_{ac}, and ω at an instability boundary. This analysis assumes that the instability envelope for the new particle is the same as that of the spherical particle. The mass thus determined can be compared with that inferred from optically sizing the levitated particle.

(*a*) *Experimental procedure*

To demonstrate the usefulness of the EDB system for studying ice we measured the growth and sublimation rates of frost crystals with various initial sizes and shapes. Each morning the chamber was carefully cleaned and loaded with DI water, closed and allowed to equilibrate thermally. The frost crystals (grown from vapour on the inside surfaces of the balance itself) were introduced into the centre of the balance using either a small stainless steel needle or a small quartz capillary vacuum manipulator. The particles typically carried a net electrostatic charge in the range 0.1–0.5 pC. Both signs of charges were seen, although most (about 80%) of the particles were positively charged. After introduction of the ice particle, the chamber was closed and the dc potential, ac potential, and ac frequency were adjusted so that the particle remained at the null point. Size and shape measurements were also made from the transverse and longitudinal shadow images obtained with the two telemicroscopic video cameras, and were tape recorded. Subsaturation conditions were obtained near the balance centre by removing IR filters and IR mirrors from the light beams illuminating the chamber, thereby increasing the temperature of the particle and the surrounding air in the chamber. Particles with hexagonal growth habits were obtained by first sublimating a frost particle to a 'seed' of linear dimension less than 10 μm and then replacing the IR filters and IR mirrors to obtain growth conditions.

The results discussed in this paper were obtained from measurements of g/s rates of frost particles. To date, we have concentrated on (i) growth of frost or ice particles grown from frost seeds and (ii) sublimation of frost particles or seed-grown ice particles achieved by exposing the particle and the surrounding vapour to IR illumination ($T_{\text{top}} - T_{\text{bottom}} \leqslant 20°\text{C}$ for all experiments).

(*b*) *Calibration of the balance constants*

The values of C_1/C_0 calculated by the relaxation method were validated experimentally from measurements of the marginal-stability envelope. For this purpose, spherical $19.7 \pm 1.7\mu$m (manufacturer's specification) diameter polystyrene latex (PSL) particles were used to locate the lowest branch of the instability curve. This was done by varying V_{ac} and measuring the ac frequency at which large-amplitude axial oscillations first appear. Figure 4 represents such data for four different PSL particles for electrode configuration $\mathscr{A}$ of Table 1. The theoretical stability characteristics of the axial Mathieu equation solution (Eq. (6)) are also plotted as the solid line in Fig. 4. All parameters needed to calculate α and β for the PSL runs are known except the balance-constant ratio C_1/C_0. The value of C_1/C_0 was chosen so the data match the Mathieu equation solution for $\alpha = 0$ (the limit in which the particle's inertia dominates drag). The experimental data deviate from the Mathieu stability curve as α increases, but the data are highly reproducible. This same deviation was reported by Davis *et al.* (1990), Rassat and Davis (1992), and Li and Davis (1995) for double-ring configurations. It appears that combined axial and radial instabilities occur at high values of α because of the support rods. For the PSLs we find that the electronically determined sizes generally agree with optically measurements to within 8%, and that charge loss for the PSLs was less than 1% per day.

A polynomial fit of the data to

$$\beta(\alpha) = A_0 + A_1\alpha + A_2\alpha^2 \tag{8}$$

is also shown as the dashed line in Fig. 4 for ring configuration $\mathscr{A}$; the values for A_0, A_1 and A_2 are given in Table 2 for both electrode configurations. Using this parameterization, α was determined from balance voltage and ac frequency measurements alone.

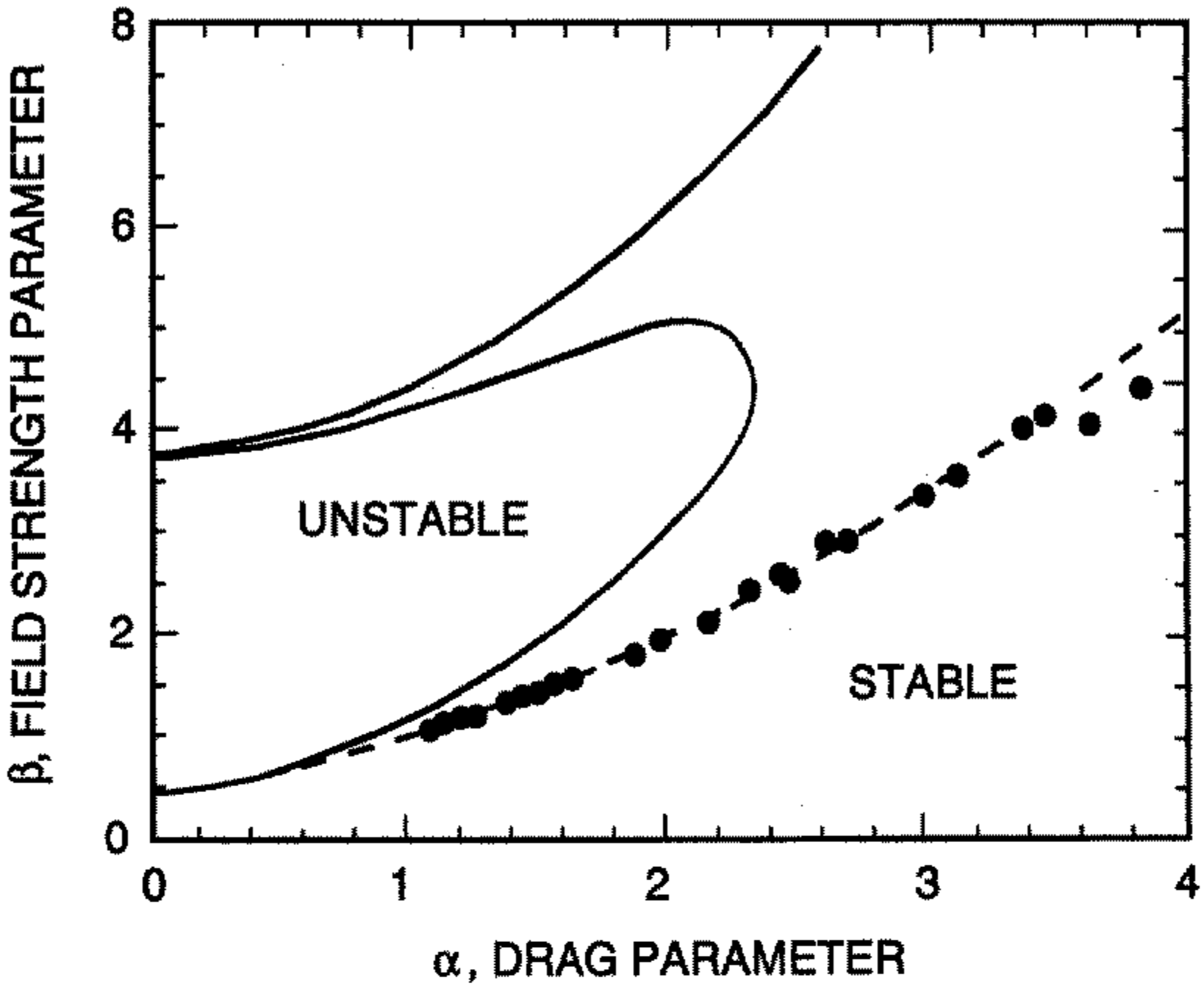

Figure 4. Axial instability envelopes, in terms of the parameters α and β defined in Eq. (7), measured for a polystyrene latex particle (plotted points, and quadratic best-fit curve using parameters given in Table 2 (dashed line)) and calculated from the Mathiew equation (6) (solid lines).

The values of C_1/C_0 inferred from the measurements for electrode configurations $\mathscr{A}$ and $\mathscr{B}$ are shown in Table 2, as well as those calculated using the relaxation code; they agree reasonably well, which gives us confidence in our calibration methods.

(*c*) *Light-scattering calibration*

For purposes of optical alignment and calibration of our light-scattering instrumentation, spherical PSL particles were levitated in the balance. Figure 5 compares the measured light-scattering intensity ($15° < \theta < 60°$) from a $19.7 \pm 1.7 \mu$m diameter PSL particle with the light-scattering intensity calculated using Mie theory for a 20.5 μm diameter sphere (the best fit). Here θ is the angle between the incident and scattered light in the horizontal plane. The agreement illustrates that a precision of a few percent is obtained by comparing the calculated and measured positions of peaks and troughs in the angular scattering profiles. Detailed comparisons between measured and calculated phase functions for spherical particles can achieve a precision of one part in 10^4 (Ray *et al.* 1991).

5. Results

(*a*) *Light-scattering measurements*

We have measured the light-scattering intensity from nearly spherical and nonspherical ice particles. This method for measuring size changes of a spherical particle is illustrated in Fig. 6, which shows two light-scattering intensities obtained from a sublimating ice particle condensed from a fog at −12°C. The size changed about 10% (from a diameter of 25.0 μm to 22.5 μm) during the 5.6 s interval between the two measurements. For

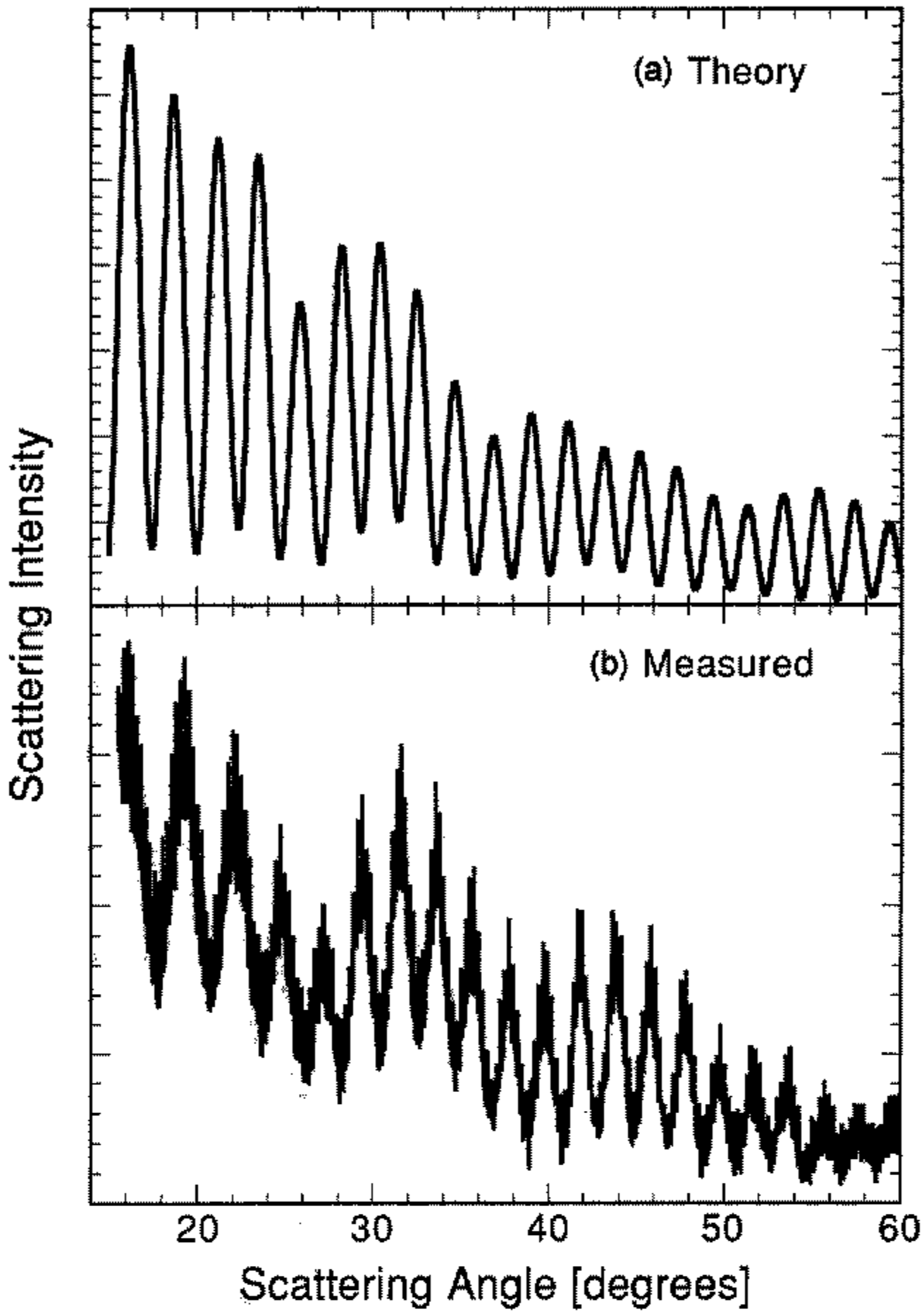

Figure 5. Light-scattering intensity as a function of scattering angle for a polystyrene latex particle, (a) calculated from Mie theory and (b) measured in the electrodynamic balance.

non-spherical particles the light-scattering data cannot be interpreted by means of classical Mie theory, so size determination must be made by balance voltage and optical-imaging measurements. A complete characterization of axisymmetric non-spherical crystals requires measurements of the scattering phase functions over a range of crystal orientations.

(*b*) *Particle mass and density determination*

Figure 7(a) shows the top and side view of an irregularly shaped frost particle when first introduced into the balance. In order to grow hexagonal columns or plates, a weak IR light source was directed at a frost particle; after 20 or more minutes the particle sublimated to a sphere or seed. The temperature at the centre of the chamber was then decreased by turning down the light source by means of IR filters/mirrors, causing the seed crystal to grow. The resulting relatively 'perfect' hexagonal column grown is shown in Fig. 7(b). The mass of the particle can be inferred from instability measurements as described above. To measure the ice density we grow a uniform hexagonal particle, set the g/s rate to zero, and measure the particle volume optically. We then measure its axial instability envelope by varying ω and V_{ac}. The effective value of ξ/ρ_{ice} is that which

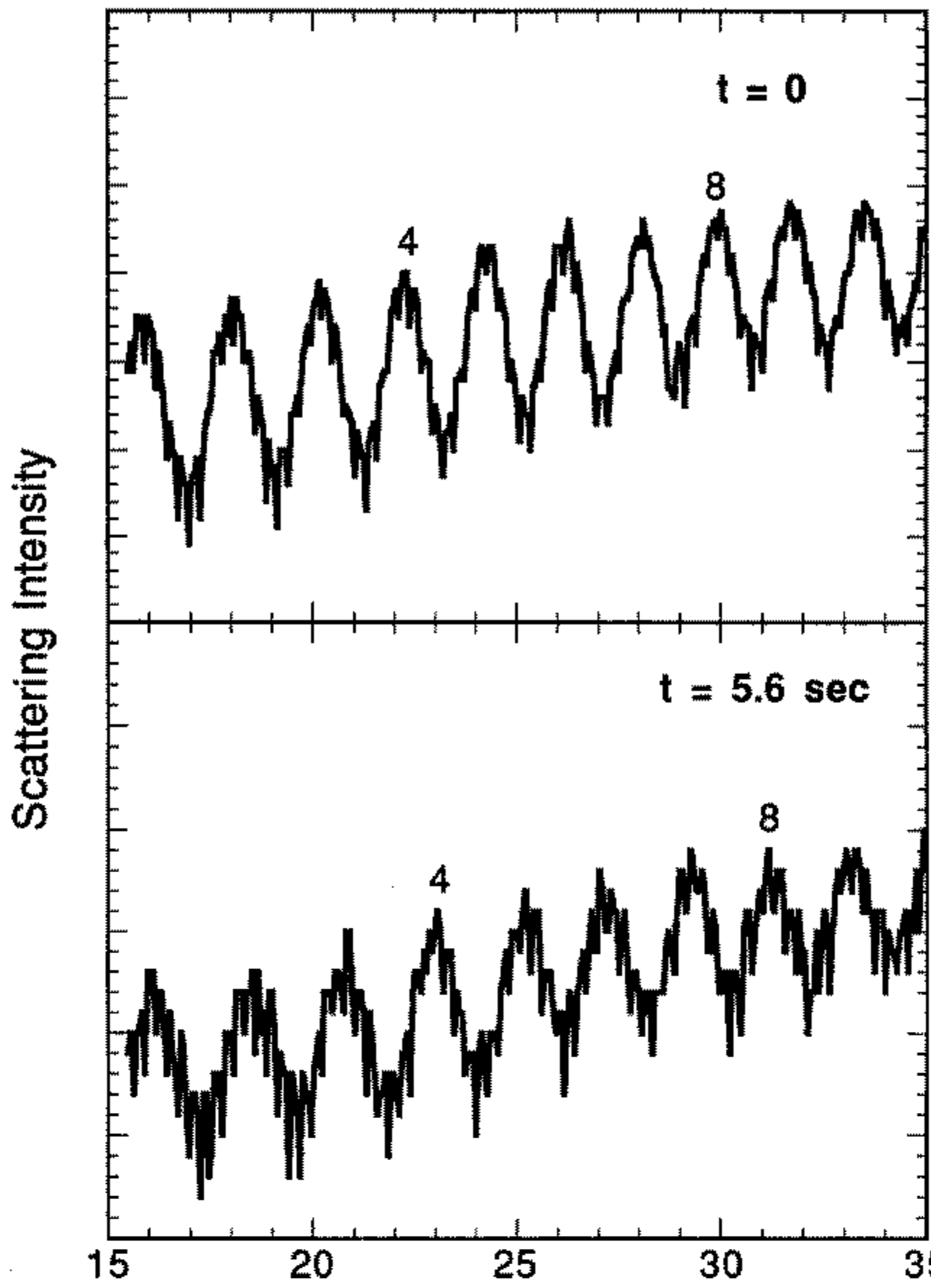

Figure 6. Scattering intensity as a function of scattering angle from a nearly spherical 25 μm ice particle condensed from a fog at -12°C. The scattering in the lower panel was measured 5.6 *s* after the upper panel. The smaller number of peaks over this angle range shows an approximate 10% decrease in particle diameter.

minimizes the difference between the ice-particle instability envelope and the instability curves for spherical PSL particles. From these values, and from drag coefficients ξ taken from published curves (e.g. Jayaweera and Cottis 1969; Locatelli and Hobbs 1974), we find that $0.7 \leqslant \rho_{ice} \leqslant 0.9$ g cm^{-3} for these particles. Over 100 frost particles with a range of initial shapes have been levitated in the balance under various temperatures between $-2 < T < -30$°C. The points in Fig. 8 are data from 14 frost particles held under various temperature and growth conditions. All of these data sets show growth of irregularly shaped frost particles without prior sublimation to a seed. After five or more minutes of growth, the resulting particle usually did not exhibit the hexagonal symmetry of the hexagonal crystal shown in Fig. 7(b), but some particles did develop facet-like surfaces near the end of the growth period. The points in Fig. 9 are data from 14 frost particles held under various temperature and sublimation conditions. All particles started with non-hexagonal frost shapes and sublimated to approximately 10 μm diameter particles with final aspect ratios appearing nearly isometric.

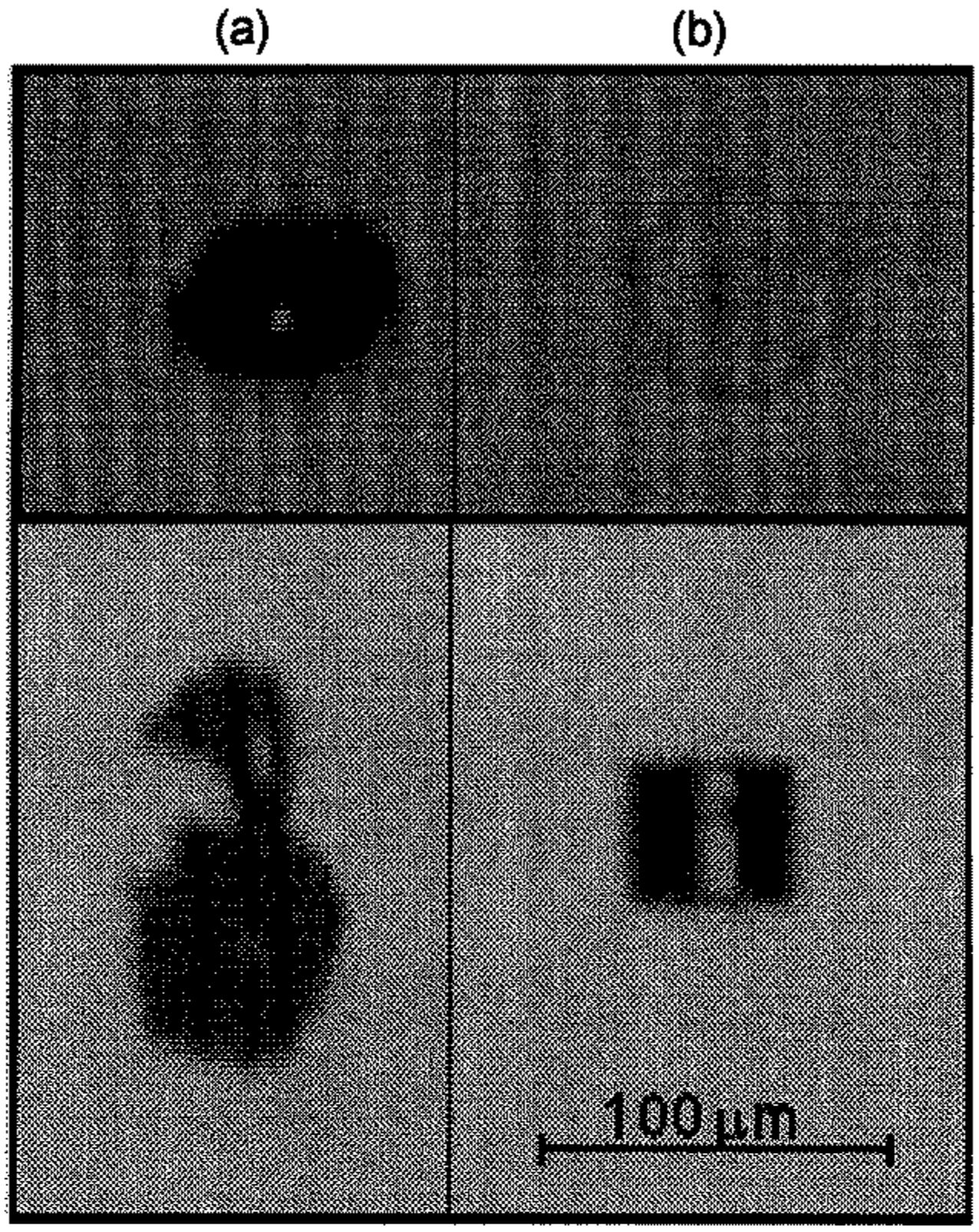

Figure 7. Pictures of the top views (upper panels) and side views (lower panels) of (a) a frost particle when first introduced into the balance and (b) a hexagonal crystal produced by sublimating a frost particle to a 'seed', followed by growth at −21°C for about 20 min. Scale line = 100 μm.

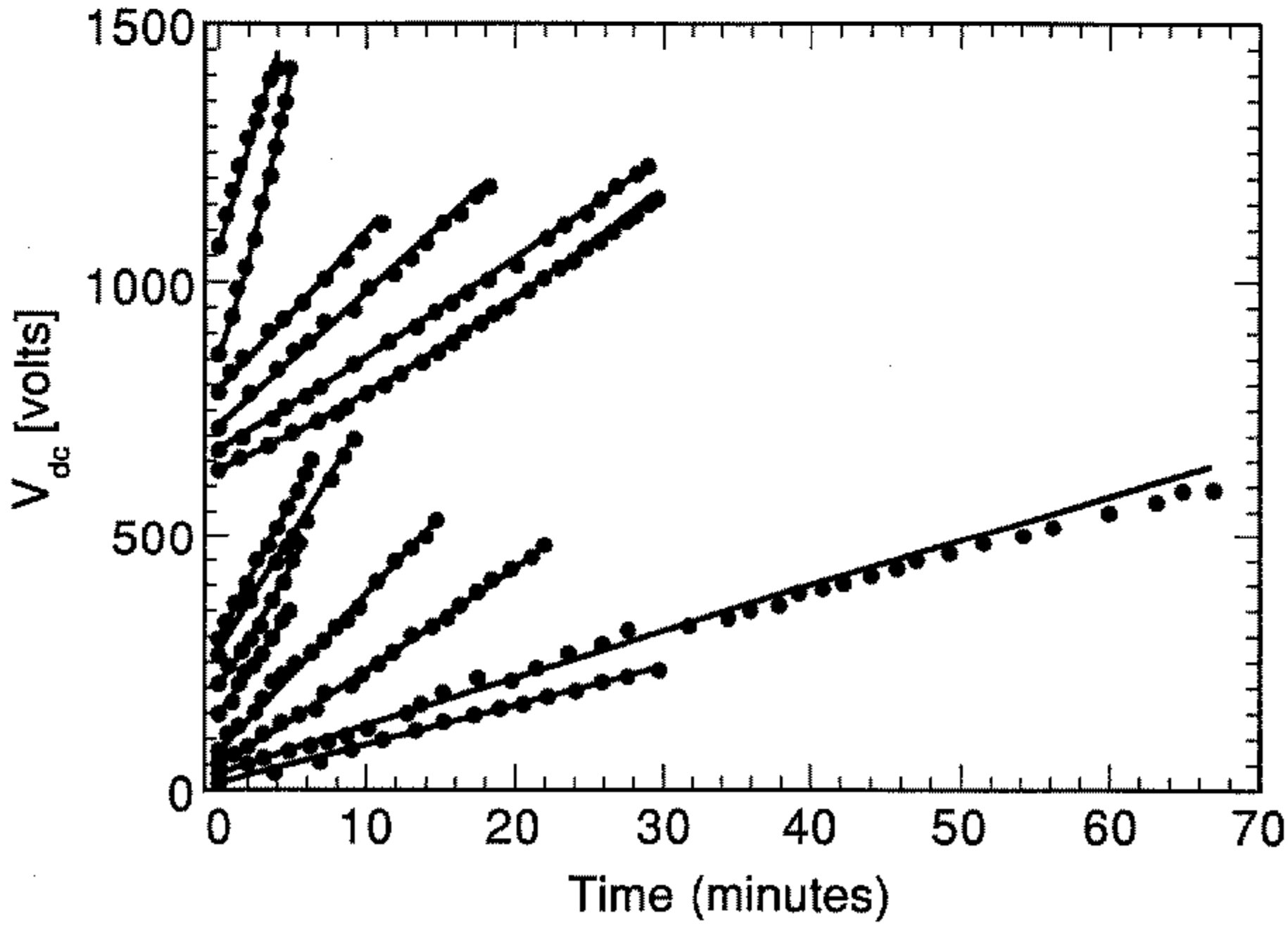

Figure 8. A plot of V_{dc} versus time for 14 growth data sets. The data sets have been shifted vertically for clarity but the changes in V_{dc} are proportional to changes in particle mass. Solid lines are the best-fit results from Eq. (18).

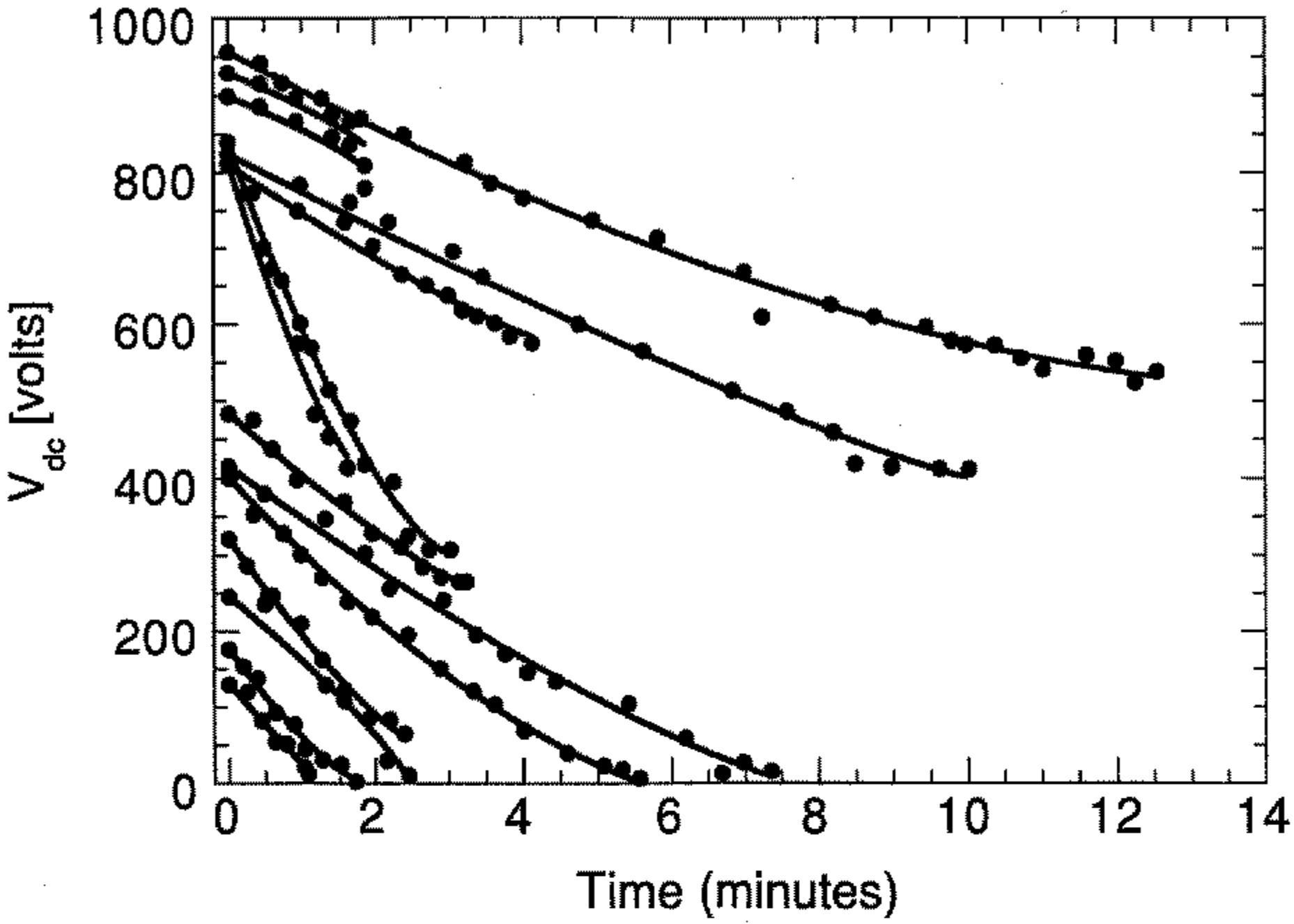

Figure 9. As Fig. 8, but for 14 sublimation data sets.

(*c*) *Growth and sublimation rates*

In the experiments to be reported here, we have measured mass gain and loss with time of a large number of ice particles. For these initial studies of mass change (as opposed to evolution of individual facets on regular crystals) it is appropriate to use the simplest model of the g/s processes, which is based on the assumptions that (i) a particle can be represented as a sphere of equivalent radius a with $m = 4\pi a^3 \rho_{\text{ice}}/3$, where ρ_{ice} is the ice density (taken to be the same for all particles), and (ii) the charge gain or loss during g/s is negligibly small, consistent with our observations. In this case, assuming the usual quasi-steady-state theory, the net vapour flux to the surface of the spherical particle is

$$F_{\text{v}} = \frac{1}{4\pi a^2}\frac{\mathrm{d}m}{\mathrm{d}t} = \frac{D}{a}\left[\rho_{\text{v}}(\infty) - \rho_{\text{v}}(a)\right], \tag{9}$$

in which $\rho_{\text{v}}(a)$ and $\rho_{\text{v}}(\infty)$ are the vapour concentrations at the surface and far from the surface, respectively, and D is the diffusion coefficient of water vapour in air at atmospheric pressure.

Analogously, the radial heat flux to the particle surface is given by

$$F_{\text{h}} = \frac{\kappa}{a}\left[T_\infty - T_a\right], \tag{10}$$

where κ is the thermal conductivity of air and T_a and T_∞ are the temperatures at the surface and far from the surface, respectively. We assume the particle is isothermal so that there is no heat flux into the particle and

$$F_{\text{h}} = -LF_{\text{v}}. \tag{11}$$

where L is the latent heat of sublimation. Equations (9), (10) and (11) are incomplete; an additional boundary condition is needed to set the conditions at the particle surface.

A number of investigators (Kuroda 1984; MacKenzie and Haynes 1992; Nelson 1995) have proposed determining this boundary condition by surface kinetics, and have studied the role of surface processes in limiting the g/s rates theoretically. For spheres (neglecting effects of surface curvature), the solution of Eqs. (9)–(11) under the assumption $T_a/T_\infty \approx 1$ yields

$$F_v = \frac{D\,\rho_{v,sat}(T_\infty)\,S_\infty}{R_o + aR_1} \tag{12}$$

where S_∞ is the supersaturation (or undersaturation) far from the crystal. The resistance to vapour and heat transport in the air, R_1, is

$$R_1 = \frac{LD\rho_{v,sat}(T_\infty)(L/RT_\infty - 1)}{\kappa T_\infty} + 1, \tag{13}$$

and R_o represents a length scale associated with the surface resistance. In this interpretation $R_o \sim 1/\gamma$, where γ is the condensation coefficient (which depends on the g/s mechanism, on temperature, and on supersaturation). Alternative interpretations and derivations of Eq. (12) have been given by Fuchs and Sutugin (1970), Pruppacher and Klett (1978) and Wagner (1982).

For $\gamma = 1$, $R_o \approx 0.1\ \mu$m , and so $R_o/aR_1 \ll 1$. In this case Eq. (12) reduces to the familiar form (with $a^2 \sim t$) for diffusion-limited growth,

$$\frac{dm^{2/3}}{dt} = f_{2/3}(T_\infty, S_\infty) \tag{14}$$

or

$$m^{2/3}(t) = m^{2/3}(0) + f_{2/3}(T_\infty, S_\infty)t. \tag{15}$$

For $R_o/aR_1 \gg 1$, Eq. (12) reduces to,

$$\frac{dm^{1/3}}{dt} = f_{1/3}(T_\infty, S_\infty) \tag{16}$$

or

$$m^{1/3}(t) = m^{1/3}(0) + f_{1/3}(T_\infty, S_\infty)t. \tag{17}$$

To determine the relative magnitudes of the resistances R_o and R_1 we compare our experimentally determined growth and sublimation curves with the generalized model

$$m^\nu(t) = m^\nu(0) + f(T_\infty, S_\infty)t, \tag{18}$$

where the exponent, ν, and the rate parameter, $f(T_\infty, S_\infty)$, are free parameters.

We first examine the observed time dependence of the size change under non-equilibrium conditions. From Eqs. (5) and (18), assuming no charge loss over the time period of each run, we can write,

$$V_{dc}^\nu = V_{dc}^\nu(0) + C(T_\infty, S_\infty)\,t, \tag{19}$$

or

$$\frac{V_{dc}}{\dot{V}_{dc}} - \left.\frac{V_{dc}}{\dot{V}_{dc}}\right|_{t=0} = \nu\,t. \tag{20}$$

where $C(T_\infty, S_\infty)$ is defined using Eqs. (5) and (12) and the dot denotes the derivative with respect to time. On the basis of the equivalent-sphere model for diffusion-limited growth we expect that $\nu = 2/3$. The individual data sets are shown in Figs. 8 and 9, where

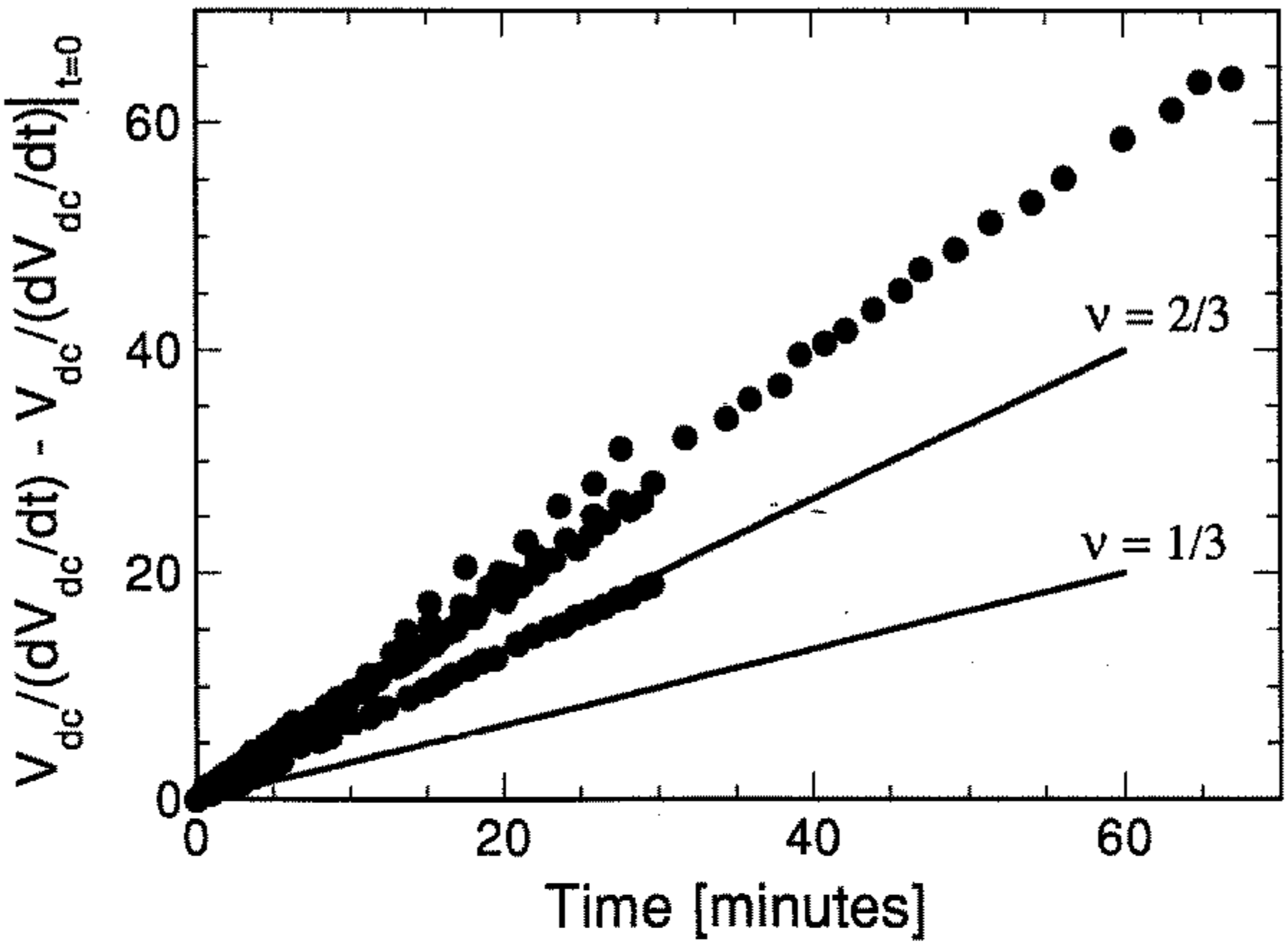

Figure 10. $V_{dc}/\dot{V}_{dc} - V_{dc}(0)/\dot{V}_{dc}(0)$ (see text) versus time (plotted points) for 14 growth and 14 sublimation data sets (see Figs. 8 and 9). The two lines have been drawn with slopes of $\nu = 1/3$ and $\nu = 2/3$. The data are consistent with $\nu = 2/3$, as predicted by Eq. (12) with $R_0 = 0$, indicating that the growth and sublimation are controlled primarily by vapour- and heat-diffusion impedances.

the lines are the fits to Eq. (19), with best-fit growth-rate parameter C and exponent ν for each data set. Each data set fits this simple parametrization quite well. The average of the best-fit exponents, $\bar{\nu}$, for the growth data is $\bar{\nu} = 0.82 \pm 0.17$, and for the sublimation data $\bar{\nu} = 0.75 \pm 0.16$. The observed g/s rates ranged from 0.004 to 0.16 μm s^{-1}. The values of $\bar{\nu}$ for both growth and sublimation are consistent with $\nu = 2/3$ (within the experimental errors). The points in Fig. 10 correspond to the 14 growth and 14 sublimation data sets of Figs. 8 and 9, replotted as $V_{dc}/\dot{V}_{dc} - V_{dc}(0)/\dot{V}_{dc}(0)$ versus t. The solid lines in Fig. 10 have the slope $\nu = 1/3$ and $\nu = 2/3$. Significant variability in the value of ν is evident in the data. A few growth data sets shown in Fig. 10 have slope $\nu = 1$, but the complete data set is consistent with the exponent $\nu = 2/3$ predicted by the simple g/s model. Within the precision of these experiments we do not detect deviations from the diffusion-limited g/s model (Eq. (14)). This is perhaps not unexpected for these particles at these temperatures and g/s rates.

To compare the measured g/s rates with our simple model, we must estimate the supersaturation at the particle position. This requires an estimate of ΔT, the change in temperature at that position due the lamp and any other heat sources or sinks not accounted for in the calculation of $T_0(0, 0)$. ΔT can be found operationally from g/s rate data. We have fitted the g/s rates of compact hexagonally symmetric crystals (not shown here) to the simple spherical model (Eq. (12)), to find a best-fit supersaturation $S_{bf}(0, 0)$. We then find ΔT from the relationship

$$S_{bf}(0, 0) = \frac{\rho_{v,0}(0, 0) - \rho_{v,sat}(T_0(0, 0) + \Delta T)}{\rho_{v,sat}(T_0(0, 0) + \Delta T)}, \tag{21}$$

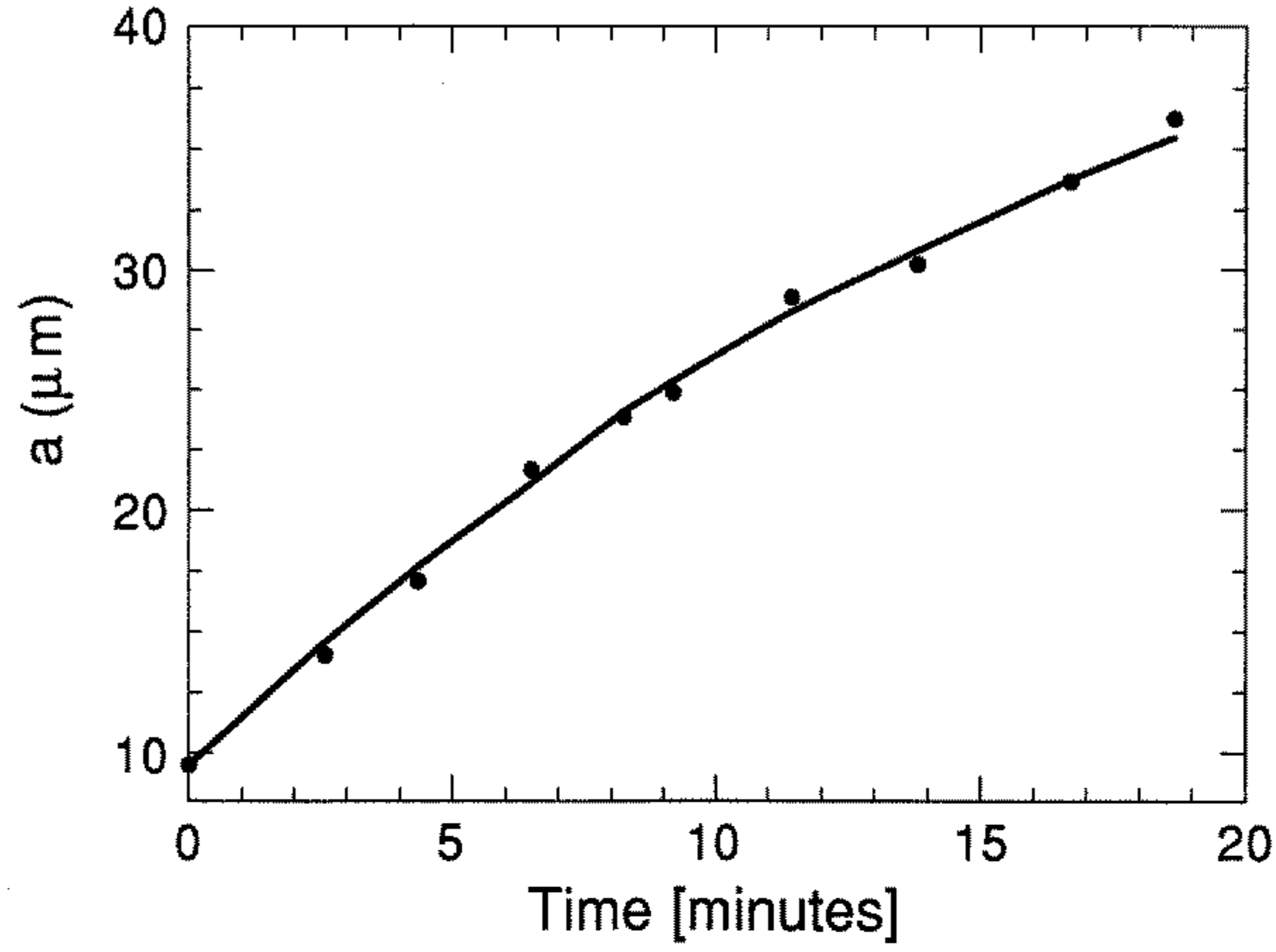

Figure 11. Particle effective radius a versus time, together with the growth and sublimation model (full line) Eq. (12) with $R_0 = 0$.

where $\rho_{v,sat}(T)$ is the equilibrium vapour density over a flat surface at temperature T and atmospheric pressure and $\rho_{v,0}(0, 0)$ is calculated analytically. The average value of ΔT thus found is approximately 0.8°C for the growth studies (IR filters/mirrors in place—IR turned down) and 1.2°C for sublimation (IR filters/mirrors removed—IR turned up). Preliminary tests with a small (300 μm) thermistor lowered into the chamber gave results broadly consistent with these. Thus we assume that the actual temperature near the particle is $T(0, 0) = T_0(0, 0) + \Delta T$. We can then use this assumption in the spherical-growth model (Eq. (12)), with the calculated vapour density $\rho_{v,0}(0, 0)$ to predict the rate of change of the equivalent radius of an irregular frost particle. This model has no free parameters and depends only on the initial particle size and the balance temperatures T_{sides}, T_{top} and T_{bottom}. Figure 11 shows a versus t for one of the ice-crystal data sets shown in Fig. 8. In this plot the solid line is obtained by the integration of Eq. (12) for the measured temperature conditions with $R_0 = 0$. Future experiments with better temperature control will provide a more accurate determination of $f(T_\infty, S_\infty)$, and we will try to determine the limits of Eq. (12) in describing g/s of non-spherical ice particles at these temperatures and in these humidity conditions. The values of S_∞ inferred from frost particle g/s rates for the data sets shown in Fig. 10 range from $-8\% < S_\infty < 1.5\%$.

6. Discussion

We have built an EDB with an internal thermal diffusion chamber to control temperature and relative humidity conditions for ice particles held between −30°C and 0°C. We introduced frost particles into this chamber and have measured the growth rates of both frost and hexagonal ice particles for mass changes by factors of ten or more. In this first

series of experiments we have demonstrated that mutually consistent values of particle size changes are inferred from (i) light-scattering phase functions, (ii) balance voltage measurements, and (iii) optical images.

In addition to these results, the EDB has afforded us the possibility of observing several features of levitated particles that have not been previously reported. We have observed that PSL particles can remain suspended for days in the EDB. This implies that the conductivity of the air in the balance is very low. We attribute this condition to the removal of ions by the ac field and the absence of a sufficiently rapid ion regeneration mechanism in the air inside the balance. We do not detect changes in ice-particle charge above a detection limit of approximately 1% per minute from the comparison of optically inferred size changes with the charge/mass ratio given by the balancing field.

During growth, some initially irregular particles developed flat facet-like features while others grew in a more shape-conserving manner. We did not distinguish particles growing in either these two modes in the data shown in Fig. 8. It is not understood why some odd-shaped frost particles change with a self-similar growth mode while others develop facet-like features. Particles that were first sublimated to a seed nearly always appeared to grow with plate-like habits when $T > -4°C$ and column-like habits when $-4 > T > -10°C$, in agreement with previous observations (Takahashi *et al.* 1991). The crystals were compact, however; aspect ratios did not rise above 1.5 or below 0.6 in these experiments. (For hexagonal-particle results see Swanson *et al.* (1998).)

During slow sublimation we have observed that (i) particles lose their initially sharp corners in accordance with previous observations, (ii) regions on the surface of particles with more curvature lose mass at about the same rate as planar regions, and (iii) about 1 in 3 particles break up as thin-neck regions develop and finally break. Specifically, we observed the break up of large-aspect-ratio prolate particles into two or more fragments, and the breaking off of small protuberances from the surface of all types of frost particles. These fragmentation processes may be partially responsible for the high concentrations of small secondary ice particles sometimes found in mixed-phase clouds. Details of these observations are reported elsewhere (Bacon *et al.* 1998a).

In section 4 we used a simple equivalent-sphere model to describe our g/s rate measurements. For faceted crystals, an expression analogous to Eq. (12) can be derived for the flux to each facet of the crystal. In this case the surface impedance varies from facet to facet and determines the evolution of particle shape in, as yet, poorly understood ways. The capacitance model (with the capacitance C replacing the particle equivalent radius a) predicts a relationship similar to Eq. (15) for compact reasonably perfect crystals. In future work we will examine the limits of applicability of these models for both growth and sublimation. We plan to use (i) a source of identically sized and identically charged particles, free of contamination and observable defects, and (ii) a reliable means of measuring humidity at the particle position. We have designed and built a droplet generator which will serve as the particle source, and are now developing an IR absorption humidity measurement instrument suitable for making measurements in the balance chamber.

Ours is the first reported g/s rate study of ice particles levitated in an EDB. Most dielectric particles rotate freely in an axisymmetric external electric field as a result of the interaction of the non-uniform field with the induced dipole in the particle. We observe that particles of sufficiently large size do not rotate in the asymmetric field near the centre of our balance, and non-spherical particles can be oriented and positioned in the EDB by adjusting the balance voltage V_{dc}, the stabilizing voltage V_{ac}, and the ac frequency ω. We plan to take advantage of this fact to study the evolution of particular facets and to measure light-scattering phase functions of hexagonal ice particles for a range of incident angles (Bacon *et al.* 1998b).

Acknowledgements

Brian Swanson and Marcia Baker are affiliated to the Geophysics Program of the University of Washington, Neil Bacon is affiliated to the Physics Department and James Davis is affiliated to the Chemical Engineering Department. Support for this research came from the Leonard X. Bosack and Bette M. Kruger Charitable Foundation, NSF Grant ATM-9417445, NSF Grant ATM-9528049, and the University of Washington Royalty Research Fund Grant 65-2622. We wish to acknowledge Li-Jen Chen for assistance with the numerical relaxation code and thank Prof David S. Covert, Prof Larry B. Sorensen and John J. Stoltenberg for providing some instrumentation used during the start-up of these experiments.

References

Aardahl, C. L., Vehring, R., Davis, E. J., Schweiger, G. and Swanson, B. D. 1997 Characterization of the electric field and particle trapping in a double-ring electrodynamic balance. *J. Aerosol Sci.*, **28,** 1491–1505

Abramowitz, M. and Stegun, I. A. 1972 *Handbook of mathematical functions*, Dover Publications Inc., New York, USA

Bacon, N. J., Swanson, B. D., Baker, M. B. and Davis, E. J. 1998a Breakup of levitated frost particles. *J. Geophys. Res.*, **103,** 13763–13775

1998b Laboratory measurements of light scattering by single ice particles. *J. Aerosol Sci.*, **29,** S1317–S1318

Baker, M. B. 1997 Cloud microphysics and climate. *Science*, **276,** 1072–1078

Baker, B., Baker, M., Jayaratne, E., Latham, J. and Saunders, C. 1987 The influence of diffusional growth rates on the charge transfer accompanying rebounding collisions between ice crystals and soft hailstones. *Q. J. R. Meteorol. Soc.*, **113,** 1193–1215

Bartlett, J. T., Van den Heuval, A. P. and Mason, B. J. 1963 The growth of ice crystals in an electric field. *J. Appl. Math. Phys.*, **14,** 599–610

Beckmann, W. 1982 Interface kinetics of the growth and evaporation of ice single crystals from the vapour phase, III. Measurements under partial pressures of nitrogen. *J. Crystal Growth*, **58,** 443–451

Beckmann, W. and Lacmann, R. 1982 Interface kinetics of the growth and evaporation of ice single crystals from the vapour phase, II. Measurements in a pure water vapour environment. *J. Crystal Growth*, **58,** 433–442

Cross, J. D. and Speare, P. A. 1969 Electrical aspects of the evaporation of ice *Brit. J. Appl. Phys.*, **2,** 1021–1025

Crowther, A. and Saunders, C. 1973 Ice crystal growth in electric fields. *J. Meteorol. Soc. Japan*, **51,** 318–324

Davis, E. J. 1992 'Microchemical engineering: The chemistry and physics of the microparticle'. In *Advances in Chemical Engineering*, **18,** Ed. J. L. Anderson, Academic Press, New York, USA

1997 A history of single aerosol particle levitation. *Aerosol Sci. Technol.*, **26,** 212–254

Davis, E. J., Buehler, M. F. and Ward, T. L. 1990 The double-ring electrodynamic balance for microparticle characterization. *Rev. Sci. Instrum.*, **61,** 1281–1288

Dong, Y.-Y and Hallett, J. 1992 Charge separation by ice and water drops during growth and evaporation. *J. Geophys. Res.*, **97,** 20361–20371

Elliot, W. P. 1971 Dimensions of thermal diffusion chambers. *J. Atmos. Sci.*, **28,** 810–811

Evans, L. 1973 The growth and fragmentation of ice crystals in an electric field. *J. Atmos. Sci.*, **30,** 1657–1664

Frickel, R. H., Shaffer, R. E. and Stamatoff, J. B. 1978 'Chambers for the electrodynamic containment of charged aerosol particles'. Report No. ARCSL-TR-77041, Chemical Systems Laboratory, Aberdeen Proving Ground, Maryland, USA

Fuchs, N. A. and Sutugin, A. G. 1970 *Highly dispersed aerosols*, Ann Arbor Science Publishing, Ann Arbor, Michigan, USA

Hartung, W. H. and Avedisian, C. T. 1992 On the electrodynamic balance. *Proc. Roy. Soc. London*, **A437,** 237–266

Jayaratne, R., Saunders, C. and Hallett, J. 1983 Laboratory studies of the charging of soft-hail during ice crystal interactions. *Q. J. R. Meteorol. Soc.*, **109,** 609–630

Jayaweera, K. O. L. F. and Cottis, R. E. 1969 Fall velocities of plate-like and columnar ice crystals. *Q. J. R. Meteorol. Soc.*, **95,** 703–709

Katz, J. L. and Mirabel, P. 1975 Calculation of supersaturation profiles in thermal diffusion cloud chambers. *J. Atmos. Sci.*, **32,** 646–562

Kuroda, T. 1984 Rate determining processes of growth of ice crystals from the vapour phase Part I: Theoretical considerations. *J. Meteorol. Soc. Japan.*, **62,** 552–561

Lamb, D. and Hobbs, P. 1971 Growth rates and habits of ice crystals grown from the vapor phase. *J. Atmos. Sci.*, **28,** 1506–1509

Lamb, D. and Scott, W. 1972 Linear growth rates of ice crystals grown from the vapor phase. *J. Crystal Growth*, **12,** 21–31

Langsdorf, A. 1936 A continuously sensitive diffusion cloud chamber. *Phys. Rev.*, **49,** 422

1939 A continuously sensitive diffusion cloud chamber. *Rev. Sci. Instrum.*, **10**, 91–103

Li, W. and Davis, E. J. 1995 Measurement of the thermophoretic force by electrodynamic levitation: Microspheres in air. *J. Aerosol Sci.*, **26,** 1063–1083

Locatelli, J. D. and Hobbs, P. V. 1974 Fall speeds and masses of solid precipitation particles. *J. Geophys. Res.*, **79,** 2185–2197

Loyalka, S. K., Tekasakul, P., Tompson, R. V. and Warder, R. C. Jr. 1995 Computation of electric fields and particle motion in electrodynamic balances. *J. Aerosol Sci.*, **26,** 445–458

MacKenzie, A. and Haynes, P. 1992 The influence of surface kinetics on the growth of stratospheric ice crystals. *J. Geophys. Res.*, **97,** 8057–8064

Nelson, J. 1995 'A theoretical study of ice crystal growth in the atmosphere'. PhD Dissertation, University of Washington, Seattle, USA

Paul, W. and Steinwedel, H. 1953 A new mass spectrometer without a magnetic field. *Zeit. Naturforsch.*, **A8,** 488–450

Pruppacher, H. R. and Klett, J. D. 1978 *Microphysics of clouds and precipitation*, D. Reidel, Dordrecht, Germany

Rassat, S. D. and Davis, E. J. 1992 Chemical reaction between sulfur dioxide and a calcium oxide aerosol particle. *J. Aerosol Sci.*, **23,** 165–180

Ray, A. K., Souyri, A., Davis, E. J. and Allen, T. M. 1991 Precision of light scattering techniques for measuring optical parameters of microspheres. *Appl. Optics*, **30,** 3974–3983

Ryan, B., Wishart, E. and Shaw, D. 1976 The growth rates and densities of ice crystals between −3°C and −21°C. *J. Atmos. Sci.*, **22,** 123–133

Sei, T. and Gonda, T. 1982 The growth mechanism and the habit change of ice crystals growing from the vapor phase. *J. Crystal Growth*, **94,** 697–707

Sloane, C. S. and Elmoursi, A. A. 1987 'Characterization of an electrodynamic balance for suspending charged droplets'. In the conference record of the 1987 IEEE industry applications meeting, Part II, IEEE, New York, USA

Swanson, B. and Baker, M. 1995 'Laboratory measurements of ice crystal evaporation rates'. In Proceedings of the AMS Conference on cloud physics, Dallas, Texas, USA

Swanson, B. D., Bacon, N. J., Davis, E. J. and Baker, M. B. 1998 'Levitated ice crystals: Laboratory measurements at ice particle breakup and growth/sublimation rates'. In Proceedings of the AMS conference on cloud physics, Everett, Washington, USA

Takahashi, T., Endoh, T., Wakahama, G. and Fukuta, N. 1991 Vapor diffusional growth of free-falling snow crystals between −3 and −23°C. *J. Meteorol. Soc. Japan*, **69,** 15–30

Tomlinson, E. M. and Fukuta, N. 1979 Aspect ratio of thermal diffusion chambers. *J. Atmos. Sci.*, **36,** 1362–1365

Wagner, P. E. 1982 'Aerosol growth by condensation'. In *Aerosol microphysics II: Chemical physics of microparticles. Topics in Current Physics*, **9,** Ed. E. H. Marlow, Springer-Verlag, Berlin, Germany

Wuerker, R. F., Shelton, H. and Langmuir, R. V. 1959 Electrodynamic containment of charged particles. *J. Appl. Phys.*, **30,** 342–349